Physical Chemistry Chemical Physics c7cp07551k

We have presented the Graphical Abstract text and image for your article below. This brief summary of your work will appear in the contents pages of the issue in which your article appears.

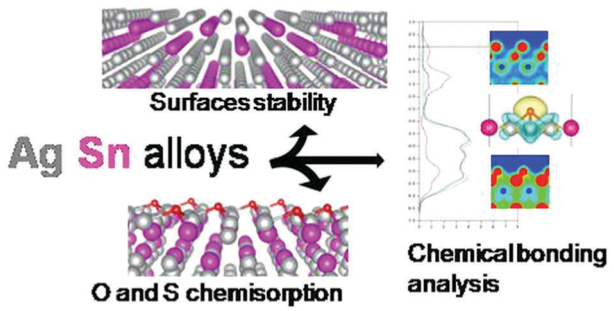

Ab initio surface properties of Ag–Sn alloys: implications for lead-free soldering

Gabriele Saleh,* Xu Chen and Stefano Sanvito

Structure, stability and reactivity of silver–tin alloy surfaces revealed using DFT calculations and discussed in the framework of lead-free soldering.

Q1

Please check this proof carefully. **Our staff will not read it in detail after you have returned it.**

Proof corrections must be returned as a single set of corrections, approved by all co-authors. No further corrections can be made after you have submitted your proof corrections as we will publish your article online as soon as possible after they are received.

Please ensure that:

- The spelling and format of all author names and affiliations are checked carefully. Names will be indexed and cited as shown on the proof, so these must be correct.
- Any funding bodies have been acknowledged appropriately.
- All of the editor's queries are answered.
- Any necessary attachments, such as updated images or ESI files, are provided.

Translation errors between word-processor files and typesetting systems can occur so the whole proof needs to be read. Please pay particular attention to: tables; equations; numerical data; figures and graphics; and references.

Please send your corrections preferably as a copy of the proof PDF with electronic notes attached or alternatively as a list of corrections – do not change the text within the PDF file or send a revised manuscript. Corrections at this stage should be minor and not involve extensive changes.

Please return your **final** corrections, where possible within **48 hours** of receipt, by e-mail to: pccp@rsc.org. If you require more time, please notify us by email.

Funder information

Providing accurate funding information will enable us to help you comply with your funders' reporting mandates. Clear acknowledgement of funder support is an important consideration in funding evaluation and can increase your chances of securing funding in the future. We work closely with Crossref to make your research discoverable through the Funding Data search tool (http://search.crossref.org/funding).

Further information on how to acknowledge your funders can be found on our webpage (http://rsc.li/funding-info).

What is Funding Data?

Funding Data (http://www.crossref.org/fundingdata/) provides a reliable way to track the impact of the work that funders support. We collect funding information from our authors and match this information to funders listed in the Crossref Funder Registry. Once an article has been matched to its funders, it is discoverable through Crossref's search interface.

PubMed Central

Accurate funder information will also help us identify articles that are mandated to be deposited in PubMed Central (PMC) and deposit these on your behalf.

Providing funder information

We have combined the information you gave us on submission with the information in your acknowledgements. This will help ensure funding information is as complete as possible and matches funders listed in the Crossref Funder Registry. **Please check that the funder names and grant numbers in the table are correct.** This table will not be included in your final PDF but we will share the data with Crossref so that your article can be found *via* the Funding Data search tool.

Funder name	Funder ID (for RSC use only)	Award/grant/contract number
H2020 Marie Skłodowska-Curie Actions	100010665	grant agreement No. 713567

If a funding organisation you included in your acknowledgements or on submission of your article is not currently listed in the registry it will not appear in the table above. We can only deposit data if funders are already listed in the Crossref Funder Registry, but we will pass all funding information on to Crossref so that additional funders can be included in future.

Researcher information

If any authors have ORCID or ResearcherID details that are not listed below, please provide these with your proof corrections. Please check that the ORCID and ResearcherID details listed below have been assigned to the correct author. Authors should have their own unique ORCID iD and should not use another researcher's, as errors will delay publication.

Please also update your account on our online manuscript submission system to add your ORCID details, which will then be automatically included in all future submissions. See here for step-by-step instructions and more information on author identifiers.

First (given) name(s)	Last (family) name(s)	ResearcherID	ORCID
Gabriele	Saleh		0000-0002-6201-9546
Xu	Chen		
Stefano	Sanvito		

Queries for the attention of the authors

Journal: **PCCP**

Paper: **c7cp07551k**

Title: ***Ab initio* surface properties of Ag–Sn alloys: implications for lead-free soldering**

For your information: You can cite this article before you receive notification of the page numbers by using the following format: (authors), Phys. Chem. Chem. Phys., (year), DOI: 10.1039/c7cp07551k.

Editor's queries are marked on your proof like this Q1, Q2, etc. and for your convenience line numbers are indicated like this 5, 10, 15, ...

Please ensure that all queries are answered when returning your proof corrections so that publication of your article is not delayed.

Query reference	Query	Remarks
Q1	Please confirm that the spelling and format of all author names is correct. Names will be indexed and cited as shown on the proof, so these must be correct. No late corrections can be made.	
Q2	Fig. 3 and 6 appear to be of low resolution and therefore appear rather blurred. Would you like to resupply the images at higher resolution (preferably as TIF files at 600 dots per inch)?	
Q3	Please note that a conflict of interest statement is required for all manuscripts. Please read our policy on Conflicts of interest (http://rsc.li/conflicts) and provide a statement with your proof corrections. If no conflicts exist, please state that ''There are no conflicts to declare''.	

PCCP

PAPER

Ab initio surface properties of Ag–Sn alloys: implications for lead-free soldering†

Cite this: DOI: 10.1039/c7cp07551k

Gabriele Saleh, *[a] Xu Chen[b] and Stefano Sanvito[a]

Received 8th November 2017,
Accepted 22nd December 2017

DOI: 10.1039/c7cp07551k

rsc.li/pccp

Ag and Sn are the major components of solder alloys adopted to assemble printed circuit boards. The qualities that make them the alloys of choice for the modern electronic industry are related to their physical and chemical properties. For corrosion resistance and solderability, surface properties are particularly important. Yet, atomic-level information about the surfaces of these alloys is not known. Here we fill this gap by presenting an extensive *ab initio* investigation of composition, energetics, structure and reactivity of Ag–Sn alloy surfaces. The structure and stability of various surfaces is evaluated, and the main factors determining the energetics of surface formation are uncovered. Oxygen and sulphur chemisorptions are studied and discussed in the framework of corrosion tendency, an important issue for printed circuit boards. Adsorption energy trends are rationalized based on the analysis of structural and electronic features.

1. Introduction

Silver and tin have constituted the major components of alloys used for assembling Printed Circuit Boards (PCBs), ever since many countries severely restricted the use of lead due to its toxicity.[1,2] In particular, Ag–Sn alloys, in combination with small amounts (<1%) of other metals such as copper, are employed as so-called lead-free solders to join the electrical components to the PCB. Moreover, both immersion Sn (ImSn) and immersion Ag (ImAg) are preferred and widely used PCB surface finishes to protect copper pads, vials and traces from corrosion and improve their solderability. However, both ImSn and ImAg finishes have their own strength and weakness, which may be overcome by using Sn–Ag as a PCB surface finish. The most relevant properties of Ag–Sn that have made them the alloys of choice to replace previously adopted Sn–Pb alloys are: low cost, suitable melting point, excellent solderability, high tensile and shear strength, and good corrosion resistance.† The latter represents a particularly important issue as many applications require PCBs to be exposed to air pollution. Corrosion-related failures are then not uncommon and represent an important economic burden for the electronic industry.

The Ag–Sn phase diagram displays two Ag-rich phases (the ε and ζ phases, whose stoichiometries roughly correspond to Ag_3Sn and Ag_4Sn, respectively) and a solubility of up to about 10% of Sn in the fcc-Ag lattice at room temperature. No stable phases exist on the Sn-rich side of the diagram, and the solubility of Ag in Sn is almost zero. The eutectic point lies at $Ag_{0.04}Sn_{0.96}$, and the corresponding solid is composed of Ag_3Sn dispersed in the Sn matrix. Commonly adopted solders have an Ag/Sn ratio close to the eutectic composition. Rapid cooling of the melt produces finely dispersed (lamellar) Ag_3Sn, while slow cooling leads to macroscopic Ag_3Sn aggregates.[3] The latter influences the mechanical properties and corrosion resistance of the alloy. Indeed, it was shown that the flash-cooled $Sn_{0.965}Ag_{0.3}Cu_{0.05}$ solder does not corrode when exposed to humid air, due to the formation of a protective SnO_x passivation layer.† In contrast, sizeable corrosion was observed when Ag_3Sn aggregates are exposed on the solder surface. The mechanism of such a corrosion phenomenon is not clear, but it was allegedly attributed to a galvanic process, similar to what occurs to Ag–Sn alloys in NaCl solution.[4,5] Noticeably, it was also inferred that Ag_3Sn crystals in the abovementioned solders decompose into a $Ag + SnO_x$ mixture upon air exposure. Studies on corrosion in pure Ag_3Sn, where galvanic corrosion can be ruled out, are not available in the literature to the best of our knowledge. Pure and Sn-doped Ag exposed to air tarnish and form Ag_2S due to a reaction with H_2S.[6] Alloys with a higher Sn content (13.5 and 15%, ζ phase) are significantly more resistant to corrosion, allegedly due to SnO_2 passivation.[6] The high reactivity of Ag towards reduced sulphur compounds is particularly problematic to the electronic industry. Conversely, Sn displays a high resistance towards those compounds, which is beneficial for the electronic industry.

Composition, structure and reactivity of surfaces determine several of the key properties of the alloys adopted in PCBs, most

[a] School of Physics, AMBER and CRANN institute, Trinity College Dublin, College Green, Dublin 2, Ireland. E-mail: gabrielesaleh@outlook.com
[b] Nokia Bell Labs, 600 Mountain Avenue, Murray Hill, NJ, USA

† Electronic supplementary information (ESI) available: Full list of surface energies, additional Ag–Sn structures, and oxygen and sulphur chemisorption energies at low coverage. See DOI: 10.1039/c7cp07551k

obviously their corrosion resistance and solderability. An atomic-level understanding of those surface features represents a fundamental starting point for the rational design of alloys with superior properties. Nonetheless, to date this information has not been known for Ag–Sn alloys.

The present work aims at filling this gap by presenting a thorough *ab initio* investigation of the Ag–Sn surfaces. We systematically explore the surface energy of all low-index surfaces in order to determine those that are most likely to form in a real sample. For the most relevant surfaces, we evaluate and provide a rationale for the chemisorption energy of oxygen and sulphur, thereby estimating the tendency of alloys to undergo corrosion. In fact, direct corrosion is a complex process that generally proceeds through the following steps: (i) physisorption of molecules, (ii) dissociation and chemisorption of molecules, (iii) diffusion of corroding agents (O and S) below the surface, (iv) formation and thickening of the oxide/sulphide layer.[7] The chemisorption of oxygen and sulphur represents a key step in the corrosion process: low adsorption energies hint towards a small thermodynamic driving force for the formation of oxide/sulphide corrosion layers. As for the surface molecular dissociation, the associated kinetic barrier is known to be proportional to the energy of the final state, namely the chemisorption energy.[8,9] Thus, O and S adsorption energies represent a good proxy for the tendency to corrosion. Here we have studied, besides pure fcc-Ag and β-Sn (that is the most stable tin phase under ambient conditions), both the ε and ζ phases. For the latter, which has Sn atoms randomly distributed at Ag sites, we investigated their preferential distribution in both bulk and surfaces. We have also included in our study a metastable $AgSn_2$ compound (taken from the AFLOW library[10]) as a model for a Sn-rich alloy.

2. Theory and methods

All the calculations were carried out with the VASP code[11] (based on Density Functional Theory, DFT), adopting the Perdew–Burke–Ernzerhof (PBE) functional[12] in the framework of the all-electron projector augmented wave (PAW) method.[13] The plane wave kinetic energy cutoff was set to 700 eV and the reciprocal space was sampled through a uniform, *Γ*-centered grid with $0.20/2\pi$ Å^{-1} point spacing.

Surfaces were simulated by cutting the crystal structure along a given (*hkl*) crystallographic plane and separating the periodic images of the resulting slabs by a 17 Å vacuum layer. In each case, we made sure that the two exposed facets were symmetry-equivalent. For such slabs, the surface energy (T = 0 K) is defined as:[14,15]

$$\gamma_{hkl} = \frac{1}{2A}\left(E_{\text{slab}} - \text{NE}_{\text{bulk}} - \sum_{i}^{\text{exc.}} N_i \Delta\mu_i\right) \quad (1)$$

where A, N and E_{slab} are respectively the surface area, the number of atoms, and the energy of a unit cell of the slab, and E_{bulk} is the energy per atom of the bulk crystal. The last term of eqn (1) accounts for an excess on the surface of N_i atoms of a given species i, with respect to the bulk stoichiometry. $\Delta\mu_i$ is the difference between E_{bulk} of the alloy and the chemical potential of the species i in the alloy A_nB, $\mu_i^{A_nB}$. The latter is generally not known, but for a stable alloy it is bounded between two values (for an alloy A_nB),[14]

$$E_{\text{A}}^{\text{pure}} + \frac{\Delta H_{\text{A}_n\text{B}}^{\text{form}}}{n} \leq \mu_{\text{A}}^{\text{A}_n\text{B}} \leq E_{\text{A}}^{\text{pure}} \quad (2)$$

where $E_{\text{A}}^{\text{pure}}$ is the energy per atom for the pure A crystal, and $\Delta H_{\text{A}_n\text{B}}^{\text{form}}$ is the formation enthalpy of the A_nB alloy. We adopted eqn (1) and (2) in calculating the surface energy as we considered, for a given *hkl* surface, all possible terminations. These include the non-stoichiometric ones that would form by exchanging atoms with the bulk, which acts as an external reservoir.‡ For the sake of conciseness, we report in this work the surface energies obtained by setting $\mu_i^{A_nB}$ exactly in between the two extremes of eqn (2). The full surface energy ranges for each surface are reported in Tables S1 and S2 (ESI†). It is worth mentioning that those ranges never exceed 2.5 and 1.2 meV Å^{-2} in Ag_3Sn and $AgSn_2$, respectively. Note that the formation enthalpies were calculated with respect to β-Sn, that is the most stable tin allotrope at ambient temperature and under the PCB operative conditions (but not at $T < 250$ K, where α-Sn is more stable), and that eqn (2) is applied to (metastable) $AgSn_2$ as well.

Surface energies calculated by extracting E_{bulk} directly from bulk calculations incorporate a non-negligible error.[15] This is related to the way the *k*-point net is generated, and it results in surface energies not converging as the slab thickness increases. The most accurate workaround was introduced by Fiorentini and Methfessel,[16] and consists in obtaining a bulk energy for each *hkl* slab from a linear fit of E_{slab} *vs.* slab-thickness. This method (referred to as 'FM' hereinafter), however, increases the computational cost of the surface energy determination by almost one order of magnitude. We applied it to the most stable surfaces of each system, while for a qualitative ranking of the surface energies we extracted E_{bulk} from bulk calculations ('direct' method). The slab thicknesses were about 20 Å for the direct method, while for the FM method we fitted the bulk energy on 4–7 points corresponding to slabs of thicknesses in the 30–40 Å range (number of points and maximum thickness chosen so as to have convergence in γ_{hkl}). For Ag_4Sn (hcp metal) and pure Ag, only the most stable surface was considered (001 and 111, respectively[17]). The *ab initio* surface energies of β-Sn have been reported previously,[18] and we included in our study the five most stable (*hkl*) orientations. For $AgSn_2$, we considered those (*khl*) surfaces where h, k and l were 0 or 1, plus the (121) surface as a visual inspection suggested it to have a low number of dangling bonds (and indeed it turned out to be quite low in energy, see Table S2, ESI†). For Ag_3Sn, given its importance in PCBs, we performed a thorough surface study by including all

‡ This is because, for a macroscopic crystal, the number of surface exposed atoms is negligible compared to the number of bulk atoms. For example, it can be easily demonstrated that for a spherical Ag particle whose radius is as small as 1 μm, only 0.04% of atoms are located on the surface.

low-index surfaces plus all the surfaces known to be energetically low for hexagonal systems: 2 prismatic, 2 basal, 2 pyramidal and 2 twinning. Note that, in the *Pmmn* space group of Ag_3Sn, there are 2 symmetry-independent crystallographic planes for each of the 8 surfaces just listed, and we included them all in our study.

The oxygen and sulphur adsorption energies were determined as:

$$E_{O_2}^{ads} = -\left(E_{O_2/slab} - E_{slab} - E_{O_2}\right); \quad (3a)$$

$$E_{S_2}^{ads} = -\left(E_{S_2/slab} - E_{slab} - 1/4E_{S8}\right). \quad (3b)$$

Here E_{slab}, E_{O_2}, and $E_{O_2/slab}$ represent the energies of, respectively, the metal slab, the free oxygen molecule (in the triplet ground state), and that of the slab where one oxygen atom is chemisorbed on two symmetry-equivalent sites on the two sides of the slab. The same definition applies to the sulphur adsorption energy, except that we considered as the reactant the well-known S_8 cyclic crown-shaped molecule (octathiocane). The adsorption sites were determined as follows. The positions of all (under-coordinated) surface atoms in the slab were projected on a plane, Delaunay triangulation was applied, and the initial adsorption sites were defined as the centre, edges and vertex of each triangle. Periodic images of atoms in neighbouring cells were also considered, so as to include triangles that cross the cell boundaries. Those initial adsorption sites that lie closer than 0.005 Å to another one, or outside the cell boundaries, were discarded. This procedure was carried out by means of an in-house built fortran code.§ A slab + oxygen system was constructed for each of those selected positions placing the O atom 1.5 Å above the adsorption site, and the adsorbate position was optimized (through VASP, see above). The resulting systems were energy ranked, and for those lower in energy (typically within 1 eV from the most stable one) a geometry optimization of all the atomic positions, hence including the slab atoms, was performed. This latter stage is repeated for sulphur, thereby assuming the energy ranking of adsorption sites to be similar between O and S (assumption verified *a posteriori*). For the relevant surfaces, we evaluated $E_{O_2}^{ads}$ and $E_{S_2}^{ads}$ at lower coverage by calculating them on a supercell of the slab with area of at least 59 $Å^2$; generally, no qualitative differences between higher and lower coverage were observed (see Tables S6 and S7, ESI†). As a final note, we mention that our Delaunay-triangulation-based procedure turned out to be similar to the one developed independently by Montoya *et al.*[19]

3. Results and discussion

3.1 Bulk structure of Ag–Sn Alloys

The ζ phase composition can range from $Ag_{0.88}Sn_{0.12}$ to $Ag_{0.77}Sn_{0.23}$ and this phase is commonly referred to as Ag_4Sn.

§ For the Delaunay triangulation subroutine, we adapted a publicly available fortran77 code written by J. Bernal from the National Institute of Standards and Technology.

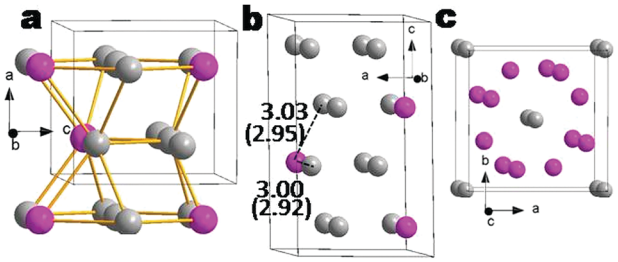

Fig. 1 Crystal structure of Ag_3Sn (a), Ag_4Sn (b) and $AgSn_2$ (c). In panel (a) the bonds are shown, highlighting the distorted hexagonal structure. In panel (b), the nearest neighbour Ag–Sn distances (in Å) are indicated, while the corresponding values in hcp-Ag are reported in parentheses. In this and in the following figures, Ag and Sn atoms are colored in grey and purple, respectively, while grey lines represent the unit cell boundaries.

It is composed of an hcp-Ag matrix where Ag atoms are disorderly substituted by Sn.[20] In order to investigate the energetics of the Sn atom distribution, we generated several representative $Ag_{13}Sn_3$ hcp supercells differing by the position of Sn atoms (see Fig. S1, ESI†). In the most stable arrangement, Sn atoms lie far apart (Fig. 1b). Indeed, Sn–Sn contacts within the hcp-Ag matrix induce a local strain that increases the energy, as the Ag–Ag nearest neighbour distances in hcp are significantly smaller than Sn–Sn in β-Sn (2.92 *vs.* 3.07 Å). In general, Sn has a covalent radius larger than Ag: the insertion of Sn in the hcp-Ag matrix induces a shift of Ag atoms away from the Sn center (Fig. 1b).

Ag_3Sn crystallizes in an orthorhombic cell (*Pmmn* space group), that is in fact a distortion of a hexagonal lattice[21] (Fig. 1a). The crystal system is therefore not dissimilar from Ag_4Sn, and accordingly no Sn–Sn contacts are present in Ag_3Sn. Finally, the structure of the model system $AgSn_2$ is reported in Fig. 1c. Our calculations reveal that this structure is less stable than the Ag_3Sn + α-Sn mixture by 11 meV per atom (at T = 0 K).

3.2 Surface energies and structures

The calculated surface energy of β-Sn is about half of that of Ag (see Table 1), as also observed experimentally.[17] Therefore, Sn-rich surfaces are expected to be more energetically favourable for Sn–Ag alloys, a fact that we observe in $AgSn_2$, where the most stable surfaces expose only Sn atoms (Fig. 2 and Table S2, ESI†). Their surface energy is close to but lower than that of Sn (Table 1). This confirms the expectation above, while also

Table 1 Surface energy of selected surfaces for the studied systems (most stable terminations)

System	Miller indices	Surface energy[a] (meV $Å^{-2}$)
β-Sn	101[b]	22.4
Ag (fcc)	111[b]	45.8
Ag_3Sn	001[b]	33.0
Ag_3Sn	100	36.5
Ag_3Sn	011	33.7
$AgSn_2$	110[b]	20.2

[a] Calculated through the FM method, see the main text. [b] Most stable surface of the corresponding element/compound.

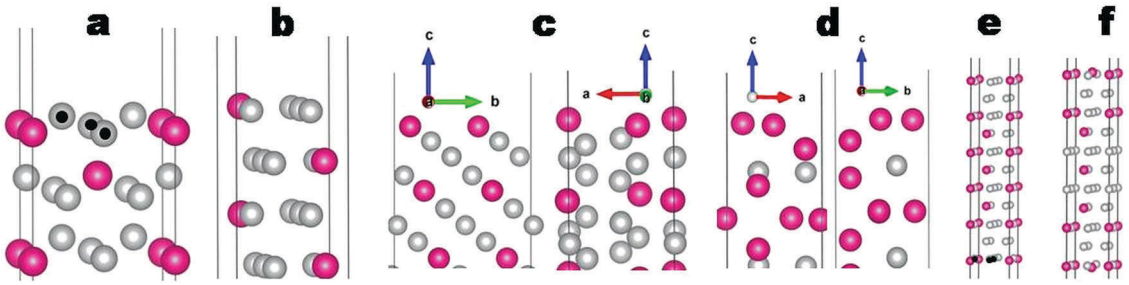

Fig. 2 Structures of selected surfaces in their most stable termination. (a) $Ag_3Sn(001)$, (b) $Ag_3Sn(100)$, (c) $Ag_3Sn(011)$, in two different orientations, (d) $AgSn_2(110)$, in two different orientations, (e) the $Ag_4Sn^{(25)}(001)$ slab, (f) the $Ag_4Sn^{(50)}(001)$ slab. In (a) and (e), black dots identify those Ag atoms that are kept at the geometry of pure Ag in the computational experiment described in Section 3.3 of the main text.

hinting for a lower energetic penalty in cleaving the Sn–Ag bonds compared to the Sn–Sn ones.

In Ag_3Sn and Ag_4Sn, the tendency of exposing Sn atoms on the surface competes with other energetic factors. For the (001) surface of Ag_4Sn, *i.e.* the most stable one for hcp-Ag, we tested a number of Sn atom arrangements, similar to what we did for the bulk. Configurations having 25% and 50% Sn atom coverage (hereinafter $Ag_4Sn^{(25)}$ and $Ag_4Sn^{(50)}$, respectively) on the surface are the most favourable and are close in energy (Table S4, ESI†). $Ag_4Sn^{(25)}$ is slightly more stable, although the energy difference (2.4 meV per surface-atom) is small compared to the room temperature thermal energy. This is despite the presence of energetically unfavourable Sn–Sn contacts in $Ag_4Sn^{(50)}$ (Fig. 2e and f). Therefore, the surface composition in $Ag_4Sn(001)$ results from a balance between two competing factors: the tendency of Sn atoms to stay far apart (steric hindrance), and that of those atoms to be on the surface (lower Sn surface energy). Overall, our calculations predict for Ag_4Sn, a preferential accumulation of Sn atoms on the surface: Sn is estimated to compose 25 to 50% of the surface atoms.

Selected Ag_3Sn surfaces are represented in Fig. 2a–c, and the surface energies are reported in Table 1 and Fig. S1 (ESI†). (100) and (001) are among the lowest energy surfaces, and in a hypothetical undistorted hexagonal Ag_3Sn they would correspond to the (0001) and (10−10) planes, respectively. The latter form the two most stable surfaces for hcp pure metals,[17] as they are the most closely packed and minimize the number of dangling bonds. The remaining low-energy surfaces are visibly less close packed (*e.g.* Fig. 2c), but they all share a common feature: a stoichiometric excess of Sn atoms (Table S1, ESI†). These results suggest that the stability of the Ag_3Sn surfaces is determined by a trade-off between the tendency of forming close packed surfaces, thus minimizing the number of dangling bonds, and that of exposing Sn atoms, so as to avoid the high energy penalty associated with the rupture of the Ag–Ag bonds (see above). This hypothesis finds confirmation in the surface energy being invariably much higher for all terminations having a stoichiometric excess of Ag atoms (Table S1, ESI†). The surface energies give us access to the most stable form of precipitate particles (within the zero-temperature approximation) through the Wulff construction,[22,23] presented in Fig. 3 for Ag_3Sn. This has a particular relevance in light of the paramount importance that Ag_3Sn (nano)particles have in lead-free soldering: plate-shaped particles form in Ag–Sn-based slowly cooled solders,[24] and their presence deteriorates the mechanical properties[25] and the corrosion resistance[3] of solders. Fig. 3 shows that there are at least 5 sets of facets (100, 001, 110, 101, and 011) that dominate the particle surface, whereas a plate-like particle would form when one surface dominates. This result indicates that even at slow cooling rates, kinetic effects play a fundamental role in the growth of Ag_3Sn nanoparticles.

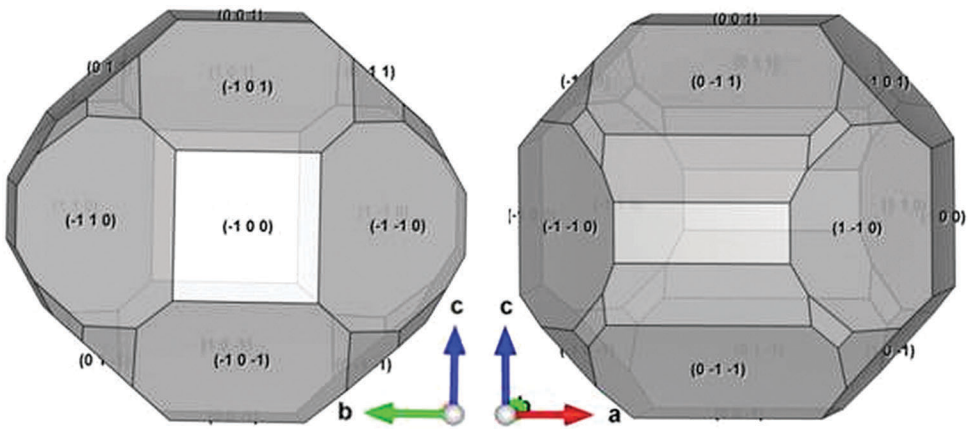

Fig. 3 Wulff construction for Ag_3Sn particles.

Concerning β-Sn, we note that our surface energy ranking differs from that of ref. 18, even when we adopt the 'direct' method (and the PBE functional[12]) as they did. We deem our calculations more reliable in light of the much larger basis set we used.¶ Moreover, in passing from the 'direct' to the FM method, swaps occur in the ranking among surfaces close in energy (in Ag_3Sn and $AgSn_2$ as well, see Tables S1–S3, ESI†). This strong sensitivity on the adopted computational approach is not surprising, as surface energy calculations from metal slabs involve energy differences in the order of meV per atom, *i.e.* well below the accuracy of commonly adopted computational approaches such as DFT. In light of this result, we conclude that differences on the order of 1% in surface energies should be regarded as non-significant.

3.3 Oxygen and sulphur adsorption energies

In this section we present the O adsorption energies ($E_{O_2}^{ads}$, eqn (3)) and we rationalize them by analyzing the structural and electronic features of the adsorbate–surface bonds. Then we discuss the differences between $E_{O_2}^{ads}$ and $E_{S_2}^{ads}$ in the framework of corrosion tendency. We place a special emphasis on how the binding energies change with the bulk and surface composition, as the strategy of tuning technologically relevant properties such as corrosion resistance by alloying is of central importance for the electronic industry and for materials design in general. We consider the following surfaces, in their most stable termination: β-Sn(100), Ag(111), $AgSn_2$(110), $AgSn_2$(100), Ag_3Sn(001), $Ag_4Sn^{(25)}$(001), $Ag_4Sn^{(50)}$(001). Moreover, we included in our study the non-close-packed Ag_3Sn(011) surface, in its Sn-richest termination. A more stable termination exists for Ag_3Sn(011), but its surface energy is comparable to that considered here (35.4 *vs.* 33.9 meV Å^{-2}, Table S1, ESI†).

Table 2 reports $E_{O_2}^{ads}$ for the investigated surfaces, while some relevant adsorption structures are shown in ~~Fig. 3~~. For all surfaces the most energetically favourable binding site is a hollow position. We ~~found~~ that allowing surface relaxation changes $E_{O_2}^{ads}$ by up to 1 eV (Table 2), yet it hardly alters the ranking among the binding sites of a given surface (Table 2). Concerning pure elements, oxygen adsorption is much more exothermic in Sn than in Ag, in accordance with the fact that the former readily and spontaneously forms oxide layers upon air exposure, while Ag_2O forms much more slowly under ambient conditions.

Hollow adsorption sites in Ag–Sn alloys can be formed by either one species only (Ag3 or Sn3 sites, see Table 2) or by a mix of Ag and Sn atoms. The fist category comprises all the sites of $AgSn_2$(100), one site in Ag_3Sn(001) and one in $Ag_4Sn^{(25)}$(001). The values of $E_{O_2}^{ads}$ in those positions can be exploited to examine to what extent the atoms other than those bonded to O influence the adsorption energies. Qualitative insights can be gained from the analysis of the charge density rearrangement upon oxygen adsorption (an example is shown in Fig. 5). We observe that the density changes are mostly confined within the

¶ We adopted a 700 eV plane-wave energy cutoff while Hormann *et al.*'s was only 220 eV. Those authors did not report the *k* mesh for surfaces, but ours was fine enough (see the 'Theory and methods' Section) to assume that no significant changes would occur in further increasing the number of *k*-points.

Table 2 Oxygen adsorption energies $E_{O_2}^{ads}$ for selected adsorption sites on the investigated surfaces

System	Surface	Site[a]	$E_{O_2}^{ads}$ (eV)	$\Delta E^{relax\,b}$ (eV)
Ag	111	Ag3[c]	1.05	0.21
Sn	100	Sn3[c]	4.05	0.71
Sn	100	Sn3	3.38	0.54
$AgSn_2$	110	Sn3[c]	3.61	0.46
$AgSn_2$	100	Sn3[c]	4.01	0.69
Ag_3Sn	001	Ag2Sn[c]	1.80	0.59
Ag_3Sn	001	Ag3	0.60	0.45
Ag_3Sn	011	AgSn2[c]	2.81	1.00
Ag_3Sn	011	Ag2Sn	2.14	0.55
$Ag_4Sn^{(25)}$	001	Ag2Sn[c]	1.61	0.25
$Ag_4Sn^{(25)}$	001	Ag3	0.18	0.20
$Ag_4Sn^{(50)}$	001	Ag2Sn	2.14	0.81
$Ag_4Sn^{(50)}$	001	AgSn2[c]	2.45	0.79

[a] The 3 atoms forming the hollow sites are indicated, see Fig. 4 and 7. [b] Difference in adsorption energy between the fully relaxed and frozen slab (see Section 2). [c] Most stable adsorption site for the corresponding surface.

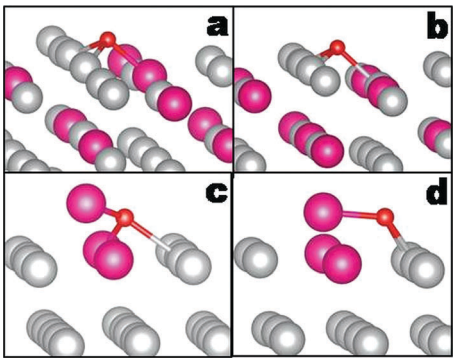

Fig. 4 Structures of oxygen adsorbed on surfaces. (a) the Ag_3Sn(001) Ag2Sn site, (b) the Ag_3Sn(001) Ag3 site, (c) the $Ag_4Sn^{(50)}$(001) AgSn2 site, (d) the $Ag_4Sn^{(50)}$(001) Ag2Sn site. Here and in Fig. 7 the adsorption sites are indicated by the atoms closest to the centre of the site (typically 3 atoms for hollow positions).

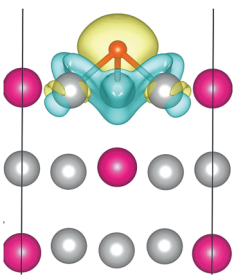

Fig. 5 Deformation density for oxygen adsorbed onto the Ag3 site of Ag_3Sn(001). The adopted isovalue is 0.01 e Bohr^{-3} (yellow = positive, blue = negative). The deformation density is defined as the difference between the charge density distribution of the slab + oxygen system and the superposition of the charge density distributions of the isolated slab and the oxygen atom in a vacuum, in the same geometry as in the slab + oxygen system.

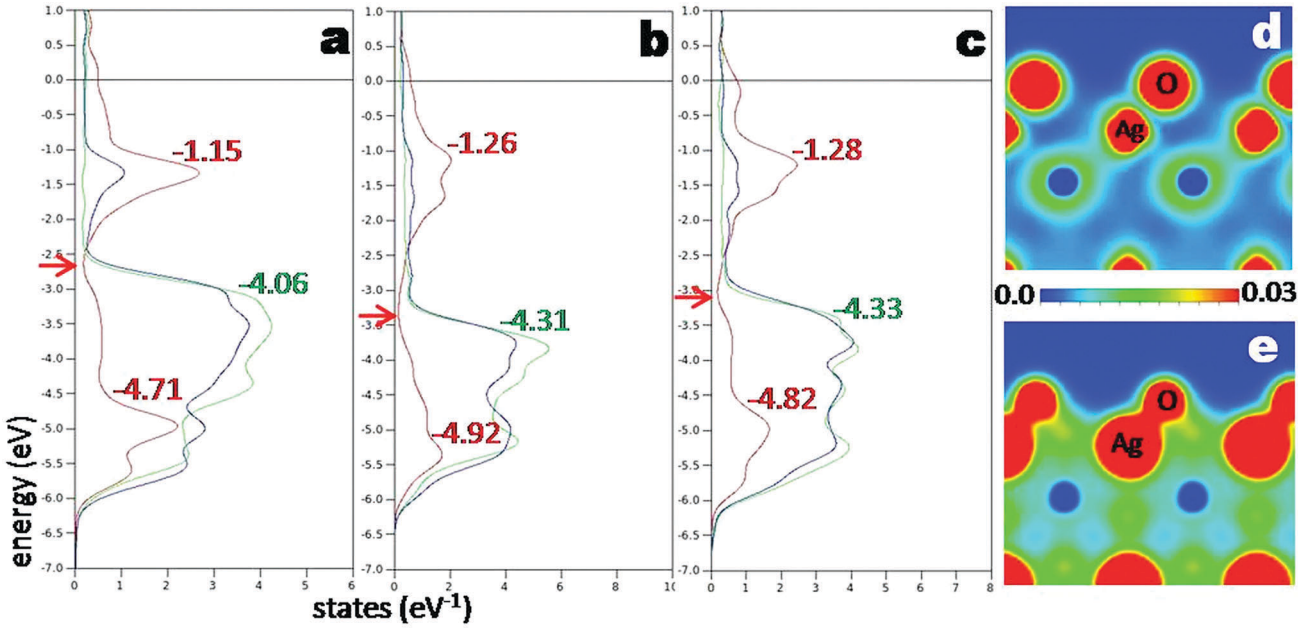

Fig. 6 *p*-DOS and partial charge density for Ag3 adsorption sites. Panels (a), (b) and (c) are the *p*-DOS of Ag(111), $Ag_3Sn(001)$ and $Ag4Sn^{(25)}(001)$, respectively; red, blue and green lines are respectively the DOS projection onto oxygen, the Ag atom bound to it, and a free surface Ag atom. Note that the metal atom positions were kept frozen at the geometries of the clean slabs, in order to single out electronic effects. The charge density distribution (e $Bohr^{-3}$) of Ag_3Sn relative to the ~~high (low)~~ O–Ag energy ~~peak is~~ reported in ~~(d and e)~~ in a plane containing the Ag–O interatomic axis. Green numbers indicate the centre of the d-band (surface Ag). Red numbers report the centre of bonding (lower) and antibonding (upper) oxygen-projected states. The integration of the oxygen contribution was carried out from the bottom of the d-band (where it vanishes) to 0.5 eV above the Fermi level. The energy level adopted as boundary between the energy ranges assigned to bonding and antibonding states is indicated by a red arrow on the energy scale of each system.

metal atoms forming the adsorption site, hinting at a negligible interaction between oxygen and the remaining metal atoms. Therefore, the atoms surrounding the oxygen binding site may only affect the adsorption energies through an indirect influence on the atoms bonded to oxygen. Moving to our quantitative results, we observe that $E_{O_2}^{ads}$ in $AgSn_2$ is close to that of Sn, although variations are observed depending on the surface orientation and binding site. This suggests that oxygen binding at Sn3 sites is weakly dependent on the environment. Conversely, Ag3 sites in Ag–Sn alloys display $E_{O_2}^{ads}$ values significantly lower than that of pure Ag. Adsorption sites formed by both Ag and Sn display $E_{O_2}^{ads}$ values in between those of pure elements, as expected.

The first step to rationalize the results presented in the paragraph above is investigating the origin of the difference in $E_{O_2}^{ads}$ of Ag3 hollow sites between Ag and Ag–Sn alloys. Two factors may lead to such a difference: structural and/or electronic. Structural effects refer to the geometry of atoms forming the (hollow) binding site and to the ability of a given surface to rearrange upon O adsorption. Instead, by 'electronic effects' we designate the influence of the identity of the atoms surrounding silver on its bond with oxygen; in other words, this term is used to indicate a lower oxygen binding ability of the Ag3 site due to changes in the band structure caused by Sn alloying. In order to disentangle these two factors, we performed the following computational experiment. In $Ag_3Sn(001)$ and $Ag_4Sn^{(25)}(001)$ we moved the 3 Ag atoms forming the Ag3 hollow site so as to have Ag–Ag distances and AgÂgAg angles as in the clean Ag surface (Fig. 2). We then optimized the slab geometry while keeping the positions of those three Ag atoms frozen.‖ In the final step, a new adsorption energy $E'^{ads}_{O_2}$ is determined by optimizing the oxygen position on the Ag3 site while keeping the slab geometry frozen. This last step in the oxygen adsorption on the frozen slab is performed on pure Ag as well, in its clean slab geometry. Similar $E'^{ads}_{O_2}$ values among Ag_3Sn, $Ag_4Sn^{(25)}$ and pure Ag would indicate that the differences in $E_{O_2}^{ads}$ of Ag3 sites (Table 2) are due to structural effects. This is not the case: the values of $E'^{ads}_{O_2}$ in Ag_3Sn and $Ag_4Sn^{(25)}$ (0.12 and 0.09 eV ~~per~~ molecule, respectively) are much lower than in pure Ag (0.96 eV ~~per~~ molecule). Therefore, the origin of the differences in adsorption energies on Ag3 sites is to be sought in the electronic structure. For that purpose, we analyzed the density of states (DOS) of the slab-oxygen systems of Ag_3Sn, $Ag_4Sn^{(25)}$ and pure Ag. First we observe the presence in the DOS of two main peaks relative to O–Ag hybridization: one at the bottom of the Ag d-band and the other in between the top of the d-band

‖ Note that to perform the computational experiment we had to adsorb the O atom on one side of the slab only, and we multiplied the value by 2 to compare it with other E_{O2}^{ads} values. This will introduce a small error due to the created dipole, but it does not affect our conclusions as they are based on qualitative considerations.

and the Fermi level. These correspond respectively to (mostly) bonding and antibonding states (Fig. 6d and e) in agreement with the well-known Hammer–Nøsrkov[26] model. The latter also establishes that the lower is the energy of the d-band centre with respect to the Fermi level, the more metal–adsorbate antibonding states are filled, hence the weaker is the metal–adsorbate bond. The d-band centre of silver and the Ag–O antibonding states shift to lower energies in passing from Ag to Ag–Sn alloys (Fig. 6). However, the differences between Ag_3Sn and Ag_4Sn are only marginal in spite of the significant disparity in $E_{O_2}^{ads}$. Therefore, we conclude that the lower $E_{O_2}^{ads}$ of Ag3 sites in Ag–Sn alloys compared to those in pure Ag is to be traced back to the Sn-induced d-band centre lowering of Ag. In contrast, the differences among the various Ag–Sn alloys are affected by the adsorption site geometry or by other fine details of the electronic structure, such as the energetics of the metal-to-oxygen charge transfer.

We rationalize $E_{O_2}^{ads}$ for mixed Ag–Sn sites by considering the recently proposed "surface mixing rule".[27] The latter states that the adsorption energy of a given alloy surface binding site can be approximated by the weighted average of the values of the forming elements. Applying such a rule as it is would lead to significant discrepancies between the predicted and calculated $E_{O_2}^{ads}$ values (Table S5, ESI†). However, if we replace the value of pure Ag with that of the Ag3 site in the alloy considered, the surface mixing rule results to be fairly successful in predicting the binding energies (Table S5, ESI†). $Ag_4Sn^{(50)}$ results anyway in having important deviations that can be traced back to the strain caused by Sn accumulation on the surface. Oxygen-bonded atoms tend to move along the surface plane upon oxygen adsorption; on close-packed surfaces, they typically drift away from the adsorbate,[28] and the entire surface rearranges consequently. In $Ag_4Sn^{(50)}$, such a displacement would shorten the Ag–Sn and Sn–Sn distances, thus increasing the strain even further (Section 3.2) and is therefore energetically unfavourable. As a result, in both Ag2Sn and AgSn2 adsorption sites, one Sn atom buckles out of the surface upon O adsorption (Fig. 4c and d), indicating a different mechanism of surface rearrangement with respect to the other investigated surfaces.

Compared to oxygen, sulphur has a lower affinity for Sn surfaces (Table 3), in agreement with the observed formation of SnO_x when tin alloys are exposed to a gas mixture containing both sulphur and oxygen.[6] Conversely, Ag displays similar O and S adsorption energies. Note that these $E_{O_2}^{ads}$ and $E_{S_2}^{ads}$ values follow the same trend of bulk sulphide and oxide formation:[29] the formation enthalpy of Ag_2O (SnO_2) is comparable to (greater than) that of Ag_2S (SnS_2). Yet, silver oxides do not grow upon air exposure, while Ag_2S readily forms when Ag is exposed to H_2S-containing air.[6] Therefore, the silver tarnishing process must be more involved than what gleaned from adsorption energies alone. For example, it may depend on the ability of silver to diffuse through the oxide or sulphide layers in order to allow the layer to grow once formed,[30] or it can be the result of reactions involving several gas-phase molecules (a more likely scenario), as discussed at the end of this section.

Sulphur adsorbs on Ag–Sn alloys less favourably than oxygen (Table 3). For Sn3 and Ag3 sites the $E_{S_2}^{ads}$ values follow the same trends as for $E_{O_2}^{ads}$. That is, for Ag3 sites the adsorption energies are lower than in pure Ag due to the Sn-induced d-band lowering, while Sn3 sites display similar $E_{S_2}^{ads}$ values between β-Sn and $AgSn_2$. The main difference with respect to oxygen concerns the Ag–Sn mixed adsorption sites, as the corresponding sulphur adsorption energies are lower than or equal to those of Ag3 sites, hence defying the 'surface mixing rule'.[27] The (011) surface of Ag_3Sn represents an exception, as it features comparatively much higher $E_{S_2}^{ads}$ values, that lie in between those of Sn and Ag pure metals (see also Table S7, ESI†). The origin of this difference can be understood by inspecting the sulphur adsorption geometries (Fig. 7). Unlike other surfaces, $Ag_3Sn(011)$ significantly rearranges upon sulphur adsorption. As a result, sulphur binds at four-atom sites, having metal–S–metal angles lower than in the other surfaces and comparable to that of oxygen (compare Fig. 7a to Fig. 7b, c and Fig. 7 to Fig. 5). Note that a similar rearrangement takes place as well upon oxygen adsorption at the AgSn2 site of $Ag_3Sn(011)$ (Fig. S3, ESI†), but in the case of oxygen the adsorption site remains unchanged. These rearrangements are important for attaining the observed high adsorption energies, especially for sulphur: indeed, among Ag–Sn alloy surfaces, $Ag_3Sn(011)$ is the one that displays the highest energy gain upon surface relaxation.

In order to rationalize these trends in $E_{S_2}^{ads}$, we take into account the following surface structural features: (i) $Ag_3Sn(011)$ is the only loosely-packed surface among those investigated, (ii) the crystal structures – and hence the geometry of hollow binding sites – of Ag_3Sn and Ag_4Sn alloys are essentially determined by the hcp-Ag lattice (see Section 3.1),** (iii) the

Table 3 Sulphur adsorption energies $E_{S_2}^{ads}$ for selected adsorption sites on the investigated surfaces

System	Surface	Site[a]	$E_{S_2}^{ads}$ (eV)	$\Delta E^{relax\,b}$ (eV)
Ag	111	Ag3[c]	1.16	0.13
Sn	100	Sn3[c]	1.30[d]	0.60
Sn	100	Sn3	1.04	0.63
$AgSn_2$	110	Sn3[c]	1.16	0.48
$AgSn_2$	100	Sn3[c]	1.30	0.50
Ag_3Sn	001	Ag2Sn[c]	0.52	0.45
Ag_3Sn	001	Ag3	0.56	0.33
Ag_3Sn	011	AgSn3[c]	1.45	0.64
Ag_3Sn	011	AgSn3	1.15	0.75
$Ag_4Sn^{(25)}$	001	Ag2Sn[c]	0.48	0.17
$Ag_4Sn^{(25)}$	001	Ag3	0.15	0.13
$Ag_4Sn^{(50)}$	001	Ag2Sn[c]	0.54	0.47
$Ag_4Sn^{(50)}$	001	AgSn2	0.14	0.32

[a] The 3 atoms forming the hollow sites are indicated, see Fig. 4 and 7. For $Ag_3Sn(011)$, the atoms within a distance of 2.8 Å from the S atom are indicated. [b] Difference in adsorption energy between the fully relaxed and frozen slab (see Section 2). [c] Most stable adsorption site for the corresponding surface. [d] Note that for Sn(100), unlike other surfaces, $E_{S_2}^{ads}$ grows significantly upon lowering the coverage (2.02 eV for a 2 × 2 supercell, see Table S6, ESI).

** This can be gleaned by considering the area of the triangles defined by the 3 atoms forming the hollow adsorption site. We provide some representative values: 3.78, 3.72, 3.69, 3.72 and 4.79 Å^2 for $Ag_3Sn(001)$ (most stable Ag2Sn binding site), $Ag_4Sn^{(50)}(001)$ (most stable AgSn2 binding site), hcp-Ag (0001), Ag(111) and Sn(100), respectively.

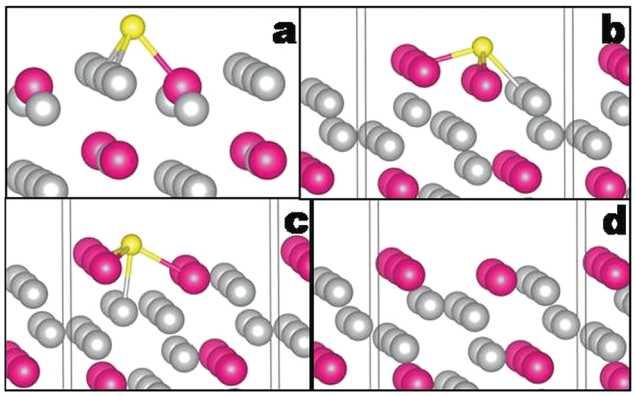

Fig. 7 Adsorption geometries for sulphur. (a) $Ag_3Sn(001)$, Ag2Sn site, (b) $Ag_3Sn(011)$, AgSn3 site, $E^{ads}_{S_2} = 1.15$ eV, (c) $Ag_3Sn(011)$, AgSn3 site, $E^{ads}_{S_2} = 1.45$. The bare $Ag_3Sn(011)$ surface is reported in (d) for comparison.

covalent radius of Sn (β-Sn) is greater than that of Ag (hcp-Ag), as shown in Section 3.1; indeed Sn–adsorbate bond lengths are generally greater than those of Ag. When considered together, features (ii) and (iii) imply that the presence of Sn in the hollow adsorption sites causes a steric hindrance and makes them less accessible by adsorbates. Given that sulphur is bigger than oxygen (ionic radii:[31] 1.84 *vs.* 1.35 Å), it experiences a greater repulsion and cannot bind effectively to Sn-containing adsorption sites, resulting in the observed low $E^{ads}_{S_2}$ values. This holds true for close-packed surfaces: loosely-packed surfaces such as $Ag_3Sn(011)$ leave more space for the adsorbate docking. Moreover, the loosely-bound nature of their surface metal atoms makes them able to rearrange so as to make the sulphur binding even more energetically favourable, while rearrangements are more energetically costly for close-packed surfaces. In order to confirm this hypothesized scenario, we evaluated the changes in adsorption energies upon application of tensile strain to 3 representative surfaces: $Ag_3Sn(100)$, Ag(111), and $Ag_3Sn(011)$ (Fig. 8). It is generally known that adsorption energies increase upon metal surface expansion (*e.g.* ref. 28). This is what we observe in Ag, where $E^{ads}_{S_2}$ and $E^{ads}_{O_2}$ increase in a similar fashion. The same increase takes place for the Ag2Sn site of $Ag_3Sn(100)$; however, the sulphur adsorption energy grows much more steadily than that of oxygen, thus confirming the role of Sn in sterically hindering the binding of larger adsorbates such as sulphur. In the loosely packed $Ag_3Sn(011)$, the adsorption energies display only small changes, even slightly decreasing for sulphur. This different behaviour can be attributed to the ability of this surface to rearrange so as to bind the adsorbate in energetically favourable positions; the adsorption site geometry (and consequently E^{ads}) does not change significantly as the surface expands (Fig. S3, ESI†). Overall, the results of Fig. 8 fully confirm the explanation provided for the sulphur binding energies. In summary, we have shown that the sulphur binding energy is low on Ag_3Sn and Ag_4Sn alloys, and we have demonstrated that this results from the steric hindrance caused by insertion of Sn into the hcp-Ag lattice. The lower sulphur adsorption energies of Ag–Sn alloys compared to pure Ag can also help in explaining the experimental result of silver tarnishing inhibition by Sn addition, although the SnO_2 passivation may also contribute to this effect. In light of the atomistic insights gained in this study, we speculate that surface defects such as steps and kinks will behave similarly to loosely-packed surfaces. In fact, both surface defects (steps and dislocations)[32,33] and non-close-packed surfaces[34] are known to be more vulnerable to corrosion.

Another striking difference between oxygen and sulphur follows from the results discussed above: sulphur adsorption energies are hardly dependent on the binding site, especially for close-packed surfaces (Table 3 and Fig. S2, ESI†). Thus, it can be inferred that sulphur has to overcome small kinetic barriers for moving across the surface. In fact, lower kinetic barriers for surface displacement of sulphur with respect to oxygen were found on nickel alloy surfaces.[35] The high surface mobility of sulphur is expected to have a number of important implications for the corrosion process. On the one hand the probability of recombination (and desorption) between chemisorbed atoms can increase, thus resulting in a corrosion slowdown. On the other hand, by being more mobile sulphur can reach more easily corrosion-sensitive areas of the material, such as surface defects, grain boundaries and loosely-packed surfaces.

Finally, it is worth discussing the dependence of the thermodynamics of chemisorption on the type of reacting molecule. In this work, the chemisorption reactions have been considered to occur between the metal surfaces and the pure elements (eqn (3a) and (3b)), so as to put oxygen and sulphur results on the same ground. However, oxidation and sulphidation can occur from other species such as H_2O and H_2S,[30] according to the reactions (*e.g.* in the case of silver):

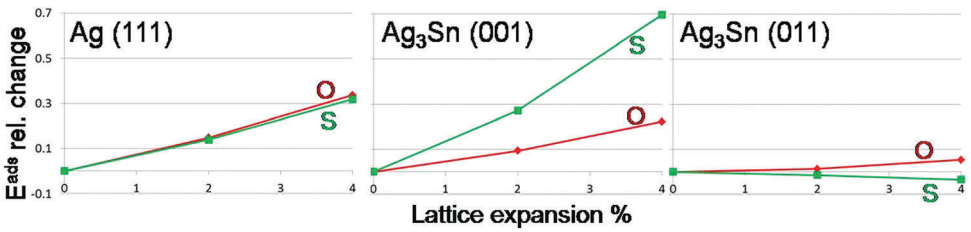

Fig. 8 Changes in oxygen and sulphur adsorption energies as a function of lattice expansion. The energy changes are expressed relative to the equilibrium geometry, *i.e.* as $(E^{eq}_{ads} - E_{ads})/E^{eq}_{ads}$, where E_{ads} is the adsorption energy at a given lattice expansion, and E^{eq}_{ads} are the values at the equilibrium lattice. The most stable adsorption site is considered in each case. The structures relative to $Ag_3Sn(011)$ are shown in Fig. S3 (ESI†).

$$Ag^{surf} + H_2O \rightarrow Ag^{surf}\text{–}O + H_2 \quad (4a)$$

$$Ag^{surf} + H_2S \rightarrow Ag^{surf}\text{–}S + H_2 \quad (4b)$$

where 'surf' indicates the metal surface. Our results indicate that these reactions are less exothermic than those between metal and the pure elements, as H_2O and H_2S have greater atomization energies than O_2 and S_8, respectively. However, processes involving several molecules are possible. In particular, in the reaction proposed in ref. 36:

$$Ag^{surf} + H_2S + 1/2O_2 \rightarrow Ag^{surf}\text{–}S + H_2O, \quad (5)$$

the sulphur adsorption is favoured by the lower binding energy of H_2S compared to H_2O. Indeed, it can be straightforwardly demonstrated that the chemisorption of sulphur through reaction (5) is more favourable than the chemisorption from S_8 by a factor $\Delta E_{form}^{H_2O-H_2S}$, where $\Delta E_{form}^{H_2O-H_2S}$ is the difference in formation energy between H_2O and H_2S (1.56 eV per adsorbed-atom, at the level of theory adopted in this work). This can also help explain why Ag_2S forms more easily than Ag_2O, in spite of similar chemisorption energies from elements and bulk formation enthalpies.

4. Conclusions and further perspectives

In the present work, DFT simulations are employed to investigate the surface properties of Ag–Sn alloys at the atomic level. In particular, we mainly address two points: the composition and stability of surfaces, and the surface adsorption energies of oxygen and sulphur. The latter is investigated and discussed in the framework of Ag–Sn corrosion, which represents an important issue for modern Ag–Sn applications in the electronic industry. The importance of the chemisorption process is twofold: it represents a proxy for the corrosion tendency, and it is a necessary step towards more involved atomistic modelling of the corrosion process.

The main factors contributing to the stability of surfaces are uncovered. As for all metals, close packed surfaces tend to be more stable. In Ag–Sn alloys, this factor competes with the tendency of exposing Sn atoms, which is a consequence of the lower Sn surface energy compared to that of Ag. In the ζ phase, where Sn atoms disorderly substitute Ag in an hcp lattice, a preferential accumulation of Sn atoms on the surface is predicted. However, a full Sn coverage on surfaces, that would minimize the surface energy, is prevented by the energetic penalty associated with the creation of Sn–Sn contacts. Indeed, our DFT simulations show that in Ag–Sn alloys Sn induces strain and local distortions due to its larger size, hence Sn atoms tend to stay separate from each other, as it also occurs in the (ordered) ε phase Ag_3Sn.

The chemisorption of oxygen and sulphur on the most stable surfaces of each of the considered alloys was studied, systematically considering all possible binding sites. In general, binding at the hollow sites is preferred. Both adsorbates bind more weakly to Ag atoms in Ag–Sn alloys as compared to pure Ag. Density of states and charge density analysis showed that this difference is due to the Sn-induced shift of the Ag d-band towards lower energy, in agreement with the well-known Hammer–Nørskov model.[26] The adsorption energies at hollow sites formed only by Sn atoms are similar in pure Sn and Ag–Sn alloys, indicating that the Sn ability to bind adsorbates does not depend significantly on the identity of the surrounding atoms. Important differences between oxygen and sulphur adsorption emerge when hollow sites formed by both Ag and Sn are considered. While the oxygen adsorption energies can be fairly well approximated by the weighted average of the adsorption energies of the elements forming the hollow binding site (surface mixing rule[27]), sulphur adsorption energies are lower than either those of the pure metals ~~or~~ all the Ag–Sn close packed surfaces. This peculiar behaviour of sulphur was demonstrated to result from its bigger size, which does not allow it to bind effectively to the surface sites formed by both Sn and Ag atoms. Implications of our results for the corrosion tendency of Ag–Sn alloys have been discussed.

Both Sn and Ag are widely used as PCB final finishes. The major weakness of using Sn as a PCB finish is the solderability degradation due to Sn–Cu intermetallic formation in the multiple assembly cycles, while Ag as a PCB finish suffers from corrosion issues in environments containing sulphur compounds. The Ag–Sn combination (especially a layered structure of Sn/Ag over Cu substrate) may provide a better PCB surface finish combining the strength of Ag and Sn as the PCB finish potentially without inheriting the weakness from either of Sn and Ag. The present work provides fundamental rationales for the Sn/Ag layered structure, namely:

1. Preferential accumulation of Sn on the surface (likely further exaggerated under ambient conditions due to the higher tendency of tin oxide formation compared to silver oxide formation).

2. Similar binding energy of oxygen towards Sn in pure Sn and SnAg alloys.

3. Reduced sulphur binding energy to Ag in SnAg alloy compared with that in pure Ag.

The above mentioned binding energies are surmised to mirror the corrosion tendency of the materials (see Introduction). We thus expect the ~~reaction~~ between the corroding agents and the layered structure (including molecular dissociation and oxide layer formation) to proceed in the same way as for pure tin. Indeed, in the Sn/Ag layered structure, Sn would act as an effective protective layer preventing silver sulphidation, while Ag will act as a barrier layer preventing Sn–Cu intermetallic formation. Experimental work is underway to verify or refute the effectiveness of this proposed layered structure as a PCB finish.

Overall, the present study uncovered the atomic-level structure of Ag–Sn surfaces, not known so far, but it also conveyed important insights about the thermodynamics of the corrosion process. More complex studies such as molecular dynamics simulations are needed in order to fully understand corrosion and other important surface processes. The results presented here may act as a springboard towards more involved

investigations, *e.g.* they can be exploited to train accurate force fields to perform mesoscale molecular dynamics simulations.

Conflicts of interest

Q3

Acknowledgements

This project has received funding from the European Union's Horizon 2020 research and innovation programme under the Marie Skłodowska-Curie grant agreement No. 713567, and from the Nokia Bell Lab. Computational resources from the Irish Centre for High-End Computing (ICHEC) and from the Trinity Center for High Performance Computing (TCHPC) are acknowledged.

References

1 Y. Zhang, in *ModernElectroplating*, ed. M. Schlesinger and M. Paunovic, John Wiley & Sons, Inc., 2010, pp. 139–204.
2 See, *e.g.*, Directive 2011/65/EU of the European Parliament, http://eur-lex.europa.eu/eli/dir/2011/65/2014-01-29.
3 M. Wang, J. Wang, H. Feng and W. Ke, *Corros. Sci.*, 2012, **63**, 20–28.
4 M. Wang, J. Wang and W. Ke, *Microelectron. Reliab.*, 2017, **73**, 69–75.
5 F. Rosalbino, E. Angelini, G. Zanicchi and R. Marazza, *Mater. Chem. Phys.*, 2008, **109**, 386–391.
6 A. A. Wronkowska and A. Wronkowski, *Corros. Sci.*, 1993, **34**, 249–259.
7 C. Gattinoni and A. Michaelides, *Surf. Sci. Rep.*, 2015, **70**, 424–447.
8 J. N. Brønsted, *Chem. Rev.*, 1928, **5**, 231.
9 M. G. Evans and M. Polanyi, *Trans. Faraday Soc.*, 1938, **34**, 11.
10 R. H. Taylor, F. Rose, C. Toher, O. Levy, K. Yang, M. Buongiorno Nardelli and S. Curtarolo, *Comput. Mater. Sci.*, 2014, **93**, 178–192.
11 G. Kresse and J. Furthmüller, *Comput. Mater. Sci.*, 1996, **6**, 15–50.
12 J. P. Perdew, K. Burke and M. Ernzerhof, *Phys. Rev. Lett.*, 1996, **77**, 3865.
13 P. E. Blöchl, *Phys. Rev. B: Condens. Matter Mater. Phys.*, 1994, **50**, 17953.
14 A. Dannenberg, M. E. Gruner, A. Hucht and P. Entel, *Phys. Rev. B: Condens. Matter Mater. Phys.*, 2009, **80**, 245438.
15 W. Sun and G. Ceder, *Surf. Sci.*, 2013, **617**, 53–59.
16 V. Fiorentini and M. Methfessel, *J. Phys.: Condens. Matter*, 1996, **8.36**, 6525.
17 L. Vitos, A. V. Ruban, H. L. Skriver and J. Kollar, *Surf. Sci.*, 1998, **411**, 186–202.
18 N. G. Hörmann, A. Gross and P. Kaghazchi, *Phys. Chem. Chem. Phys.*, 2015, **17**, 5569–5573.
19 J. H. Montoya and K. A. Persson, *npj Comput. Mater.*, 2017, **3**, 1.
20 J. Liang, C. Liao, Y. Tang, C. Yin, Y. Han, L. Nong and S. Xie, *J. Alloys Compd.*, 2010, **502**, 68–73.
21 P. J. Rossi, N. Zotov and E. J. Mittemeijer, *Z. Kristallogr. – Cryst. Mater.*, 2016, **231**, 1–9.
22 G. Wulff, *Z. Kristallogr.*, 1901, **34**, 449–530.
23 E. Clouet, M. Nastar and C. Sigli, *Phys. Rev. B: Condens. Matter Mater. Phys.*, 2004, **69**, 064109.
24 J. Shen, Y. C. Liu, H. X. Gao, C. Wei and Y. Q. Yang, *J. Electron. Mater.*, 2005, **34**, 1591–1597.
25 D. W. Henderson, T. Gosselin, A. Sarkhel, S. K. Kang, W.-K. Choi, D.-Y. Shih, C. Goldsmith and K. J. Puttlitz, *J. Mater. Res.*, 2002, **17**, 2775–2778.
26 B. Hammer and J. Nørskov, *Adv. Catal.*, 2000, **45**, 71–129.
27 J. Ko, H. Kwon, H. Kang, B. K. Kim and J. W. Han, *Phys. Chem. Chem. Phys.*, 2015, **17**, 3123–3130.
28 W.-X. Li, C. Stampfl and M. Scheffler, *Phys. Rev. B: Condens. Matter Mater. Phys.*, 2002, **65.7**, 075407.
29 O. Kubaschewski and C. B. Alcock, *Metallurgical thermochemistry, International series on materials science and technology*, Pergamon Press Inc., New York, USA, 1979, vol. 24.
30 J. P. Franey, G. W. Kammlott and T. E. Graedel, *Corros. Sci.*, 1985, **25**, 133–143.
31 R. D. Shannon, *Acta Crystallogr., Sect. A: Cryst. Phys., Diffr., Theor. Gen. Crystallogr.*, 1976, **32**, 751–767.
32 C. Heine, B. Eren, B. A. Lechner and M. Salmeron, *Surf. Sci.*, 2016, **652**, 51–57.
33 C. i. Carlisle, T. Fujimoto, W. S. Sim and D. A. King, *Surf. Sci.*, 2000, **470**, 15–31.
34 R. Xin, Y. Luo, A. Zuo, J. Gao and Q. Liu, *Mater. Lett.*, 2012, **72**, 1–4.
35 V. Alexandrov, M. L. Sushko, D. K. Schreiber, S. M. Bruemmer and K. M. Rosso, *Corros. Sci.*, 2016, **113**, 26–30.
36 J. L. Elechiguerra, L. Larios-Lopez, C. Liu, D. Garcia-Gutierrez, A. Camacho-Bragado and M. J. Yacaman, *Chem. Mater.*, 2005, **17**, 6042–6052.

